

Non-Hermitian mosaic Aubry-Andre-Harper model

Yingshixiang Wang(王应时翔), Dongze Song(宋东泽), and Xu Xia(夏旭)
Citation: Chin. Phys. B, 2025, 34 (**9**): 090201. DOI: 10.1088/1674-1056/add901
http://cpb.iphy.ac.cn; http://iopscience.iop.org/cpb

What follows is a list of articles you may be interested in

Coherent states associated with integral multi-index Mittag-Leffler functions

Dušan Popov1,2,
Chin. Phys. B, 2025, 34 (**6**): 060201. DOI: 10.1088/1674-1056/adc65d

Interaction solutions and localized waves to the (2+1)-dimensional Hirota-Satsuma-Ito equation with variable coefficient

Xinying Yan(闫鑫颖), Jinzhou Liu(刘锦洲), and Xiangpeng Xin(辛祥鹏)
Chin. Phys. B, 2023, 32 (**7**): 070201. DOI: 10.1088/1674-1056/acb9f2

Furi-Martelli-Vignoli spectrum and Feng spectrum of nonlinear block operator matrices

Xiao-Mei Dong(董小梅), De-Yu Wu(吴德玉), and Alatancang Chen(陈阿拉坦仓)
Chin. Phys. B, 2021, 30 (**4**): 040201. DOI: 10.1088/1674-1056/abd7df

Factorization method for inverse obstacle scattering problem in three-dimensional planar acoustic waveguides

Xue Qin(秦雪)
Chin. Phys. B, 2018, 27 (**10**): 100203. DOI: 10.1088/1674-1056/27/10/100203

Third-order nonlinear differential operators preserving invariant subspaces of maximal dimension

Qu Gai-Zhu (屈改珠), Zhang Shun-Li (张顺利), Li Yao-Long (李尧龙)
Chin. Phys. B, 2014, 23 (**11**): 110202. DOI: 10.1088/1674-1056/23/11/110202

Non-Hermitian mosaic Aubry–Andre–Harper model

Yingshixiang Wang(王应时翔)[1,2], Dongze Song(宋东泽)[1,2], and Xu Xia(夏旭)[1,†]

[1] *Academy of Mathematics and Systems Science, Chinese Academy of Sciences, Beijing* 100190, *China*
[2] *University of Chinese Academy of Sciences, Beijing* 100190, *China*

(Received 25 March 2025; revised manuscript received 30 April 2025; accepted manuscript online 15 May 2025)

We focus on a modified version of the non-Hermitian Aubry–Andre–Harper (AAH) model, which has garnered significant attention due to its ability to investigate localization phenomena, metal–insulator transitions, and topological phase transitions. We have made two key modifications to the non-Hermitian AAH model: First, we introduce a mosaic structure that allows for the mixing of localized and extended states, resulting in the appearance of mobility edges, which is a feature that is not present in the original non-Hermitian AAH model. In the insulating phase, leveraging Fields Medal winner Avila's global theory, our work derives a theoretical description of the localization length, a crucial parameter previously unavailable in the non-Hermitian AAH model, and obtains the exact expression for mobility edges. We studied the variation of the energy spectrum with the amplitude and quantitatively determined the topological phase transition point within the spectrum. Furthermore, we introduced an asymmetric parameter g and calculated its corresponding localization length, the location of mobility edges, as well as the precise expressions for its extended and localized states. By quantitatively calculating the Lyapunov exponent of dual models, our work reveals an interesting fact about the robustness of localized states: within an appropriate relationship between g and the coupling potential strength, the localized states exhibit similar characteristics to those in the mosaic non-Hermitian AAH model. Our work offers a more complete and nuanced understanding of localization phenomena in disordered non-Hermitian systems, paving the way for further research in this promising field.

Keywords: disordered non-Hermitian systems, mosaic structure, mobility edge

PACS: 02.30.Tb, 02.70.Hm, 72.20.Ee, 72.15.Rn

DOI: 10.1088/1674-1056/add901 **CSTR:** 32038.14.CPB.add901

1. Introduction

Anderson localization is a well-known phenomenon that refers to the disappearance of wave diffusion in disordered systems.[1] In one-dimensional (1D) and two-dimensional (2D) structures, all eigenstates are exponentially localized due to the presence of random disorder according to scaling theory of localization.[2] In three-dimensional (3D) systems, there is a mobility edge that tells apart the localized state from the extended state in the energy spectrum.[2–5]

Nevertheless, this result is not correct in quasi-periodic systems and it has been observed that lattices with periodic disorder can exhibit metal–insulator transitions in one dimension.[6] A famous example is the Aubry–Andre model, which demonstrates how the localization–delocalization transition can be derived from the symmetry parameter.[7] In this model, all single-particle eigenstates in the spectrum suddenly localize exponentially above the disorder threshold level, with the absence of a mobility edge.

As a key concept in disordered systems, the mobility edge separates the extended and localized single-particle states in the energy spectrum, which may lead to some fundamental physics,[8] such as the metal–insulator transition and thermoelectric response.[9–11] Recent studies have explored mobility edges in certain quasi-periodic 1D lattices, demonstrating generalized Aubry–Andre self-duality and making it possible to examine mobility edges in 1D structures without resorting to 3D models.[12] These studies have also looked into the role of particle interactions and many-body localization in such structures.

On the other hand, non-Hermiticity[6,13–16] has become a prominent phenomenon in modern condensed matter physics. Particularly noteworthy in the field of non-Hermitian physics is the non-Hermitian skin effect.[17,18] These research advancements have not only expanded our understanding of topology and non-Hermitian physics but also provided a theoretical foundation for designing and implementing novel topological quantum devices and functional materials. By delving into the topological properties and boundary phenomena of non-Hermitian systems, we can better grasp the unique characteristics of materials and explore new avenues and methods for achieving more efficient energy transfer, quantum computing, information storage, and other applications. The eigenvalue spectrum of non-Hermitian Hamiltonians heavily relies on boundary conditions due to their non-Bloch nature.[17–25] As a result, the mobility edge has drawn significant attention and sparked extensive research from many scholars.[17] Recent studies have highlighted and demonstrated the connection between the winding number and the skin effect.[20,21,24,25] This finding holds significant importance for understanding

†Corresponding author. E-mail: xiaxu14@mails.ucas.ac.cn

© 2025 Chinese Physical Society and IOP Publishing Ltd. All rights, including for text and data mining, AI training, and similar technologies, are reserved.

the topological properties and boundary phenomena in non-Hermitian systems.

The introduction of non-Hermiticity has brought forth new challenges and opportunities in the field of condensed matter physics. It not only enriches our understanding of topological physics but also reveals the profound connection between non-Hermitian systems and topological properties.

Extensive research has been conducted on topological phases and phase transitions in non-Hermitian free fermion systems. Longhi proposed a non-Hermitian version of the Aubry–Andre–Harper (AAH) model,[26] which, however, lacked mobility edges. To address this limitation, we introduced a mosaic structure to the non-Hermitian AAH model. In doing so, we not only determined the mobility edges of this modified model, but also derived an analytical expression for the localization length of the insulating phase, which was a crucial parameter absent in the original non-Hermitian AAH model.[26] By applying Avila's global theory,[20] we obtained a theoretical description of the localization length, thereby offering a more comprehensive and detailed understanding of localization phenomena in disordered non-Hermitian systems. What is more, the introduction of non-Hermiticity not only comes from on-site disorder's complexity, but also comes from asymmetric hopping amplitudes. Therefore, we further introduce an asymmetric parameter g into the model and investigated the quantitative influence of g on the position of the mobility edge and the energy spectrum, and found localized states' robustness.

The rest of the paper is organized as follows. We first introduce the mosaic structure in the non-Hermitian AAH model and accurately calculate its Lyapunov exponent and mobility edge in Section 2, then devoted to investigating the variation of energy spectrum with the coupling potential strength and the calculation of two topological phase transition points and presents a possible experimental scheme. In Section 3, we introduce the asymmetric parameter g, and calculate the model's localization length and location of mobility edges, and give the precise expressions of its extended state and local state. A brief conclusion is presented in Section 4.

2. Non-Hermitian mosaic AAH model

2.1. Model, energy spectrum, and mobility edge

We consider the mosaic extension of the non-Hermitian AAH model on a 1D tight-binding lattice with nearest-neighbor hopping, described by the Hamiltonian

$$\begin{cases} \hat{\boldsymbol{H}}\psi_{2n} = \psi_{2n-1} + \psi_{2n+1} + \lambda\, \mathrm{e}^{\mathrm{i}(\theta+n\alpha)}\psi_{2n}, \\ \hat{\boldsymbol{H}}\psi_{2n+1} = \psi_{2n} + \psi_{2n+2}, \end{cases} \tag{1}$$

where ψ_n is the occupation amplitudes at the various sites of the lattice, and the onsite complex potential is $\lambda\, \mathrm{e}^{\mathrm{i}(\theta+n\alpha)}$ when site is even and 0 when site is odd with amplitude λ. α is an irrational for incommensurate potentials and θ is the initial phase. Such a mosaic non-Hermitian AAH model can be obtained from the famous non-Hermitian AAH model by limiting even sites' onsite complex potential to 0.

It can be proved by direct calculation that any eigenstate $E = x + \mathrm{i}y$ of this model satisfies (see Appendix A for details):

$$\begin{cases} [-2,2] \cap \left[-\dfrac{1}{\lambda}, \dfrac{1}{\lambda}\right], & |E| < \dfrac{1}{|\lambda|}, \\ \{x + \mathrm{i}y | \dfrac{(x^2-y^2-2)^2(x^2+y^2)}{(|\lambda|(x^2+y^2)+1/|\lambda|)^2} + \dfrac{4x^2y^2(x^2+y^2)}{(|\lambda|(x^2+y^2)-1/|\lambda|)^2} = 1\}, & |E| > \dfrac{1}{|\lambda|}. \end{cases} \tag{2}$$

A key quantity for analyzing whether an energy is a localized state or an extended state is Lyapunov exponent $L(E)$. $L(E)$ is defined as follows:

$$L(E) = \lim_{n\to\infty} \frac{1}{n} \|T_n(E)\|, \tag{3}$$

where $T_n(E)$ represents the transfer matrix

$$T_n(E) = \prod_{i=1}^{n} \begin{pmatrix} E - V_j & -1 \\ 1 & 0 \end{pmatrix}, \tag{4}$$

where V_j represents the j-th site onsite potential, and $\|A\|$ represents the standard matrix norm, that is, the maximum eigenvalue of matrix $\sqrt{AA^{\mathrm{T}}}$. A useful fact about Lyapunov exponent that is repeatedly used in this article is

$$L(E) = -\lim_{n\to\infty} \frac{1}{n} \left\| \frac{\psi_n}{\psi_0} \right\|, \tag{5}$$

where ψ represents the eigenstate with E, and this formula rigorously explains the distinct physical meaning of $L(E)$: exponential decay rate of the eigenstate of E.

Using Avila's global theory, the Lyapunov exponent of model 1 at energy E is

$$L(E) = \max\left\{ \frac{\ln|\lambda E|}{2}, \frac{\ln\left|\dfrac{E^2-2}{2} + \dfrac{\sqrt{(E^2-2)^2-4}}{2}\right|}{2} \right\},$$

and especially, $\max\{0, \ln|\lambda E|/2\}$ for E in energy spectrum of $\hat{H}$, and so the mobility edge of model 1 is (see Appendix B for details)

$$|\lambda E| = 1. \tag{6}$$

To support the analytical conclusions, we carried out nu-

merical simulations of the energy spectrum and associated eigenstates of the mosaic non-Hermitian AAH model. Under periodic boundary conditions, we diagonalize the Hamiltonian on a finite lattice with a sizable $L = 400$ of sites. For this purpose, the sequence $\alpha_n = p_n/p_{n+1}$, where $p_n = 0, 1, 1, 2, 3, 5, 8, 13, 21, 34, 55, 89, 144, \ldots$ are the Fibonacci numbers, approximates the irrational $\alpha = (\sqrt{5}-1)/2$. The inverse participation ratio (IPR) of distinct eigenstates ψ_n is used to differentiate between localized and extended states, where IPR is defined as

$$\mathrm{IPR}(E) = \frac{\sum_{n=1}^{L} |\psi_n|^4}{\left(\sum_{n=1}^{L} |\psi_n|^2\right)^2}, \tag{7}$$

where ψ is the eigenstate with eigenvalue E. In contrast to a localized state, the IPR of an extended state scales as L^{-1} in the thermodynamic limit of $L \to \infty$.

For increasing values of λ, we display in Fig. 1, the numerically computed the real part of energy spectrum and IPR of the Hamiltonian. The numerical results clearly show the emergence of two distinct phases and the presence of mobility edges in the complex energy plane and are in great agreement with the analytical results. What is more, it can be seen that there is always an extended state in the system, which is different from the standard AAH model.

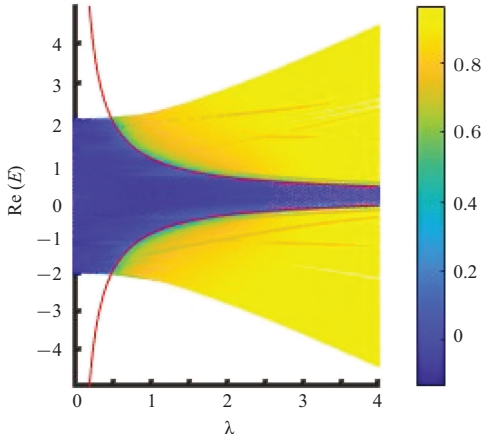


Fig. 1. The real part of the eigenvalues of model 1 and IPR as a function of λ. The color depth in the color bar indicates the size of IPR. The total number of sites is set to be $L = 400$, and α is set to be $(\sqrt{5}-1)/2$, θ is set to be 0. The red line is the curve $|\lambda E| = 1$. Our experiment shows that the red line separates the localized state and the extended state, *i.e.*, it is the mobility edge of model 1.

2.2. Topological phase transition

We carried out numerical computations of the energy spectra of the non-Hermitian mosaic AAH model for an increasing value of the typical λ to support the analytical conclusions. The numerical results show the appearance of three distinct phases, the presence of mobility edges in the complex energy plane, and their topological characterization based on the winding numbers associated with the complex spectrum of localized states, all in excellent agreement with the analytical results.

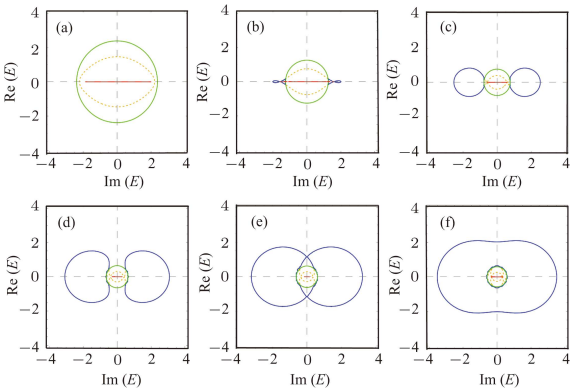


Fig. 2. Energy spectrum of our model under different λ in a lattice comprising $L = 400$ sites with periodic boundary conditions for $\alpha = (\sqrt{5}-1)/2$, $\theta = 0$: (a) $\lambda = 0.3$, (b) $\lambda = 0.51$, (c) $\lambda = 1$, (d) $\lambda = 2.5$, (e) $\lambda = 2.599$, and (f) $\lambda = 3$, the green line represents the circumference $x^2 + y^2 = 1/\lambda^2$, blue curve and red line segments show the energy spectrum of our model, whereas the dashed line represents the curve $\{x + \mathrm{i}y | \frac{(x^2-y^2-2)^2(x^2+y^2)}{(|\lambda|(x^2+y^2)+1/|\lambda|)^2} + \frac{4x^2y^2(x^2+y^2)}{(|\lambda|(x^2+y^2)-1/|\lambda|)^2} = 1, \lambda^2(x^2+y^2) \leq 1\}$.

Typical shapes of the curve $E = E(\lambda)$ for increasing values of λ are shown in Fig. 2. When λ is less than 0.5, $E(\lambda)$ is a line segment on the real axis. When $0.5 < \lambda < \lambda_1 \approx 2.598$, $E(\lambda)$ is a line segment whose two endpoints are connected to a closed loop, and the closed loops do not intersect. See Appendix C for details on the calculation of λ_1. When $\lambda > \lambda_1$, $E(\lambda)$ describes two closed loops. One of the closed loops contains another closed loop inside, and there is a line segment in the small closed loop. What is more, it is easy to see that the bigger circle will have a topological approach to the circle $x^2 + y^2 = \lambda^2$ as $\lambda \to \infty$.

2.3. An experimental scheme

Similar to Ref. [13], we can use optical pulses to walk in discrete quantum lines of coupled photonic grid lattice to simulate our model and observe the non-Hermitian effect in our model. The quantum walk is realized in a coupled fiber loop with unbalanced path length, which is used to split an optical pulse into three optical pulses, and the interval length is $\Delta L/c$. By properly adjusting EOM and AOM in the interferometer, we can simulate the Schrodinger operator with quite arbitrary potential and infer the non-Hermitian effect

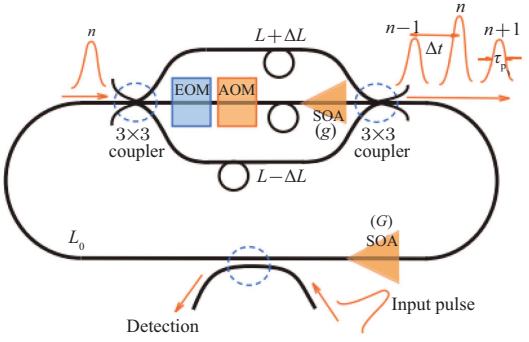


Fig. 3. The illustration of optical experiment.

of our model by analyzing the data at the output port. The experimental setup is illustrated in Fig. 3. See Appendix D for details.

3. Asymmetric hopping amplitudes

Another reason for non-Hermiticity behavior is asymmetric hopping amplitudes, to consider the impact of asymmetric jump amplitude on our model, we introduce the asymmetric parameter g, and consider the new model, which is described by the Hamiltonian

$$\begin{cases} \hat{\boldsymbol{H}}_1\psi_{2n} = \mathrm{e}^{-g}\psi_{2n-1} + \mathrm{e}^{g}\psi_{2n+1} + \lambda\,\mathrm{e}^{\mathrm{i}(\theta+n\alpha)}\psi_{2n}, \\ \hat{\boldsymbol{H}}_1\psi_{2n+1} = \mathrm{e}^{-g}\psi_{2n} + \mathrm{e}^{g}\psi_{2n+2}. \end{cases} \tag{8}$$

To consider the energy spectrum of $\hat{\boldsymbol{H}}_1$, consider its characteristic equation

$$\begin{cases} \mathrm{e}^{-g}\psi_{2n-1} + \mathrm{e}^{g}\psi_{2n+1} + \lambda\,\mathrm{e}^{\mathrm{i}(\theta+n\alpha)}\psi_{2n} = E\psi_{2n}, \\ \mathrm{e}^{-g}\psi_{2n} + \mathrm{e}^{g}\psi_{2n+2} = E\psi_{2n+1}. \end{cases} \tag{9}$$

By substituting the second item into the first item, we can obtain the following equation:

$$\mathrm{e}^{-2g}\psi_{2n-2} + \mathrm{e}^{2g}\psi_{2n+2} + \lambda E\,\mathrm{e}^{\mathrm{i}(\theta+n\alpha)}\psi_{2n} = \left(E^2-2\right)\psi_{2n}. \tag{10}$$

Consider the discrete Fourier transform

$$\begin{aligned} \psi_{2n} &= \frac{1}{\sqrt{L}}\sum_{l=1}^{L}\varphi_l \exp(\mathrm{i}\alpha l n), \\ \varphi_n &= \frac{1}{\sqrt{L}}\sum_{l=1}^{L}\psi_{2l}\exp(-\mathrm{i}\alpha l n). \end{aligned} \tag{11}$$

So the corresponding characteristic equation in momentum space is

$$(\mathrm{e}^{-2g}\mathrm{e}^{-\mathrm{i}n\alpha} + \mathrm{e}^{2g}\mathrm{e}^{\mathrm{i}n\alpha})\varphi_n + \lambda E\,\mathrm{e}^{\mathrm{i}\theta}\varphi_{n-1} = (E^2-2)\varphi_n. \tag{12}$$

Direct calculations show that

$$L(E) = -\log|\lambda E| + \max\left\{2g,\ 2\left|\,\mathrm{Im}\arccos\frac{E}{2}\right|\right\}.$$

See Appendix E for details. So if $|\lambda E| \le \mathrm{e}^{2g}$, φ cannot be an extent states, and when $\lambda E \ge \mathrm{e}^{2g}$, E is an extent state if and only if

$$2|\,\mathrm{Im}\arccos\frac{E}{2}| = \log|\lambda E|\,. \tag{13}$$

This is exactly the extent states when $g = 0$.

Return to $\hat{\boldsymbol{H}}_1$, we can see that when $|\lambda E| \le \mathrm{e}^{2g}$, E is not localized states of $\hat{\boldsymbol{H}}_1$ and when $|\lambda E| > \mathrm{e}^{2g}$, E is localized states of $\hat{\boldsymbol{H}}_1$ only if E is localized states for $\hat{\boldsymbol{H}}_1$ with $g = 0$, *i.e.*, $E = x + \mathrm{i}y$ satisfies

$$\frac{(x^2-y^2-2)^2(x^2+y^2)}{(|\lambda|(x^2+y^2)+1/|\lambda|)^2} + \frac{4x^2y^2(x^2+y^2)}{(|\lambda|(x^2+y^2)-1/|\lambda|)^2} = 1. \tag{14}$$

Thus, the mobility edge of the model has the following expression:

$$|\lambda E| = \mathrm{e}^{2g}. \tag{15}$$

Our simulations at $g = 0.5$ confirmed this, with the relevant results shown in Fig. 4.

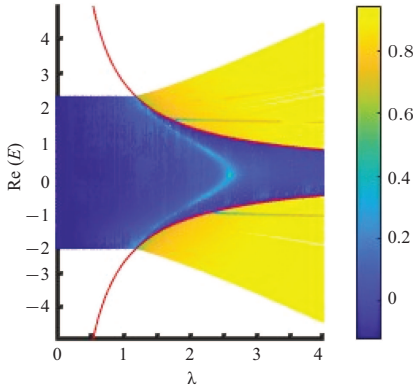


Fig. 4. The real part of eigenvalues of Eq. (9) and IPR as a function of λ. In this simulation, we set $g = 0.5$, the total number of sites is $L = 400$, $\alpha = (\sqrt{5}-1)/2$. Different colors of the eigenvalue curves indicate different magnitudes of the IPR of the corresponding wave functions. The blue eigenvalue curves denote the delocalized states and the bright yellow eigenvalue curves denote the localized states. The red lines represent the curve $|\lambda E| = \mathrm{e}^{2g}$ and we can see that it is overlapped with the mobility edge.

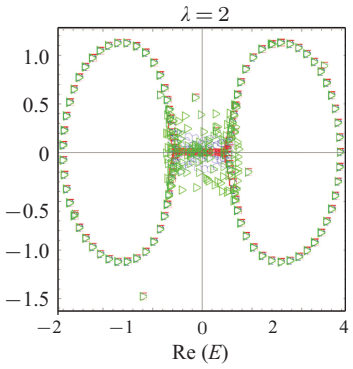


Fig. 5. Spectrum of the $\hat{\boldsymbol{H}}_1$ under different g. In this simulation, we set the total number of sites as $L = 400$, $\alpha = (\sqrt{5}-1)/2$. The red square marks represent the spectrum of $\hat{\boldsymbol{H}}_1$ when g=0, the blue pentagon represents $g = 0.5$, and the green triangle represents $g = 1$. It can be seen that as g increases, more localized eigenstates become extended states, while the remaining localized eigenstates always overlap with the localized eigenstates of $\hat{\boldsymbol{H}}_1$ with $g = 0$.

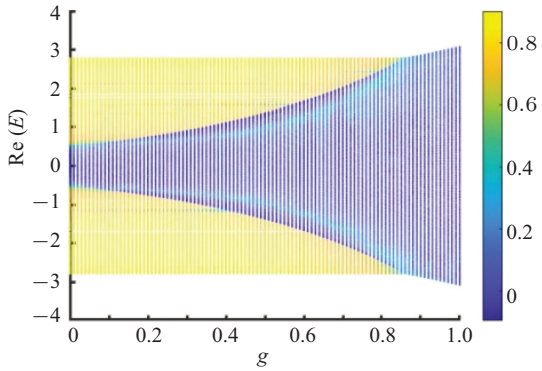


Fig. 6. The real part of eigenvalues of Eq. (8) and IPR as a function of g. The color depth in the color bar indicates the size of IPR. The total number of sites is set to be $L = 400$, α is set to be $(\sqrt{5}-1)/2$, θ is set to be 0, and λ is set to be 2. It can be seen that as g increases, the number of localized states will continue to decrease and eventually they disappear entirely.

What is more, we can see the influence of the parameter g on the energy spectrum of $\hat{\boldsymbol{H}}_1$: as g increases, more and more localized states become extended states, and the energy of the remaining localized states must also be the localized states of the $\hat{\boldsymbol{H}}_1$ with $g=0$. So, if g is sufficiently small, then the localized state will not change and on the other hand if g is sufficiently large, the localized state disappears, and the energy spectrum will only contain extended states that form an ellipse. The numerical results, presented in Figs. 5 and 6, validate this assertion.

4. Conclusion

In summary, we present a non-Hermitian extension mosaic form of a well-known quantum chaos model, the AAH model. In contrast to the non-mosaic non-Hermitian AAH model, its mosaic character extension shows a richer scenario with local–non-local phase transitions realized through the topological mobility edges of the complex energy surface. Our results provide a rather unique example of a non-Hermitian system with non-periodic order and may have interesting extensions, for example in the study of phase transitions and topological properties of integrable models of 2D NH-like crystals, as well as potential relevance in the study of quantum dynamics and quantum chaos in non-Hermitian Floquet systems. For the asymmetric model with asymmetric parameter g, we calculated its mobility edge $|\lambda E| = \mathrm{e}^{2g}$, and gave the precise expressions of its extended states and localized states. Its point spectrum is always contained by the point spectrum of the original model and when g is sufficiently large, all localized states disappear. Finally, considering the various irrational numbers that the NH extensions of the AAH model have, as well as the more joined mosaic forms, may lead to more interesting properties.

Appendix A: The expression of eigenstate

We have the following result about the non-Hermitian AAH model: any eigenstate E of AAH model satisfies

$$\begin{cases} [-2,2], & |\lambda|<1, \\ \left\{x+\mathrm{i}y \,\middle|\, \dfrac{x^2}{(|\lambda|+1/|\lambda|)^2}+\dfrac{y^2}{(|\lambda|-1/|\lambda|)^2}=1\right\}, & \\ |\lambda|>1. & \end{cases} \tag{A1}$$

Note that the eigenvalue equation for model 1 reads

$$\begin{cases} \psi_{2n-1}+\psi_{2n+1}+\lambda\,\mathrm{e}^{\mathrm{i}(\theta+n\alpha)}\psi_{2n}=E\psi_{2n}, \\ \psi_{2n}+\psi_{2n+2}=E\psi_{2n+1}. \end{cases} \tag{A2}$$

By substituting the second item into the first item, we can obtain the following equation:

$$\psi_{2n-2}+\psi_{2n+2}+\lambda E\,\mathrm{e}^{\mathrm{i}(\theta+n\alpha)}\psi_{2n}=\left(E^2-2\right)\psi_{2n}, \tag{A3}$$

so we can get that any eigenstate $E=x+\mathrm{i}y$ of our mosaic model satisfies

$$\begin{cases} [-2,2]\cap\left[-\dfrac{1}{\lambda},\dfrac{1}{\lambda}\right], & |E|<\dfrac{1}{|\lambda|}, \\ \left\{x+\mathrm{i}y \,\middle|\, \dfrac{\left(x^2-y^2-2\right)^2\left(x^2+y^2\right)}{\left(|\lambda|\left(x^2+y^2\right)+1/|\lambda|\right)^2} \right. & \\ \left. +\dfrac{4x^2y^2\left(x^2+y^2\right)}{\left(|\lambda|\left(x^2+y^2\right)-1/|\lambda|\right)^2}=1\right\}, & |E|>\dfrac{1}{|\lambda|}. \end{cases} \tag{A4}$$

Appendix B : Calculation of the Lyapunov exponent for model 1

Avila's global theory shows that, if $\hat{\boldsymbol{H}}$ is a complexed analytic Hamiltonian, if we denote $\hat{\boldsymbol{H}}_\varepsilon(x)=\hat{\boldsymbol{H}}(x+\mathrm{i}\varepsilon)$, then we can see the Lyapunov exponent $L_{\hat{\boldsymbol{H}}_\varepsilon}(E)$ of $\hat{\boldsymbol{H}}_\varepsilon$ at energy E as the function of ε_0 and it can be seen that it is a convex function and what is more, if we define a function

$$\omega(E)=\lim_{\varepsilon\to 0^+}\frac{L_{\hat{\boldsymbol{H}}_\varepsilon}(E)-L_{\hat{\boldsymbol{H}}}(E)}{2\pi\varepsilon}, \tag{B1}$$

then its value is always an integer, we call ω the acceleration.

Our mosaic Hamiltonian $\hat{\boldsymbol{H}}$ is not analytic, but we can consider its two-step combined version and consider the matrix value mapping

$$\begin{aligned} &T:\theta\in\mathbb{T}=\mathbb{R}/\mathbb{Z}\to \mathrm{SL}(2,\mathbb{C}), \\ &T(\theta)=\begin{pmatrix} E-\lambda\,\mathrm{e}^{\mathrm{i}\theta} & -1 \\ 1 & 0 \end{pmatrix}\begin{pmatrix} E & -1 \\ 1 & 0 \end{pmatrix} \\ &\quad=\begin{pmatrix} E^2-\lambda E\,\mathrm{e}^{\mathrm{i}\theta}-1 & -E+\lambda\,\mathrm{e}^{\mathrm{i}\theta} \\ E & -1 \end{pmatrix}, \end{aligned}$$

so for $\varepsilon\in\mathbb{R}$, one has

$$\begin{aligned} T(\theta+\mathrm{i}\varepsilon)&=\begin{pmatrix} E^2-\lambda E\,\mathrm{e}^{\mathrm{i}(\theta+\mathrm{i}\varepsilon)}-1 & -E+\lambda\,\mathrm{e}^{\mathrm{i}(\theta+\mathrm{i}\varepsilon)} \\ E & -1 \end{pmatrix} \\ &=\lambda\,\mathrm{e}^{-\varepsilon+\mathrm{i}\theta}\left(A_\infty+o(1)\right), \end{aligned} \tag{B2}$$

as $\varepsilon\to-\infty$, where

$$A_\infty=\begin{pmatrix} -E & 1 \\ 0 & 0 \end{pmatrix}. \tag{B3}$$

So by the continuity of the Lyapunov exponent $L_{\hat{\boldsymbol{H}}_\varepsilon}(E)$ and its derivative's quantized nature, we have

$$2L_{\hat{\boldsymbol{H}}_\varepsilon}(E)=-\varepsilon+\ln|\lambda E|, \tag{B4}$$

when $\varepsilon\to-\infty$. What is more,

$$T(\theta+\mathrm{i}\varepsilon)\to\begin{pmatrix} E^2-1 & -E \\ E & -1 \end{pmatrix}$$

as $\varepsilon\to\infty$. So

$$2L_{\hat{\boldsymbol{H}}_\varepsilon}(E)=\ln\left|\frac{E^2-2}{2}+\frac{\sqrt{(E^2-2)^2-4}}{2}\right|, \tag{B5}$$

when ε sufficiently large. Noting that $L(E+\mathrm{i}\varepsilon)$ is convex, we have

$$L(E)=\max\left\{\frac{\ln|\lambda E|}{2},\frac{\ln\left|\frac{E^2-2}{2}+\frac{\sqrt{(E^2-2)^2-4}}{2}\right|}{2}\right\}. \tag{B6}$$

Especially,

$$L(E)=\max\left\{\frac{\ln|\lambda E|}{2},0\right\} \tag{B7}$$

for E in the spectrum of our model 1.

Appendix C : Calculation of topological deformation critical point

We observe the intersection point of $\Sigma\left(\tilde{H}_{\lambda,\omega,\alpha}\right)$ with the y axis on the $|E|>1/\lambda$ part, and obtain the equation

$$y^6+\left(4-\lambda^2\right)y^4+2y^2-\frac{1}{\lambda^2}=0. \tag{C1}$$

Consider the equation

$$y^3+\left(4-\lambda^2\right)y^2+2y-\frac{1}{\lambda^2}=0. \tag{C2}$$

The derivative of the cubic curve is

$$3y^2+2\left(4-\lambda^2\right)y+2. \tag{C3}$$

So when the discriminant of the quadratic function is not negative, that is, $\lambda\notin\left(\sqrt{4-\sqrt{6}},\sqrt{4+\sqrt{6}}\right)$, the two extreme points of the cubic curve are

$$y_1=\frac{\lambda^2-4-\sqrt{\lambda^4-8\lambda^2+10}}{3}, \tag{C4}$$

$$y_2=\frac{\lambda^2-4+\sqrt{\lambda^4-8\lambda^2+10}}{3}. \tag{C5}$$

The critical case should satisfy the condition that y_2 is the double root of the equation $y^3+\left(4-\lambda^2\right)y^2+2y-1/\lambda^2=0$, thus λ_1 should be the solution to the following equation:

$$\frac{2\lambda^2-8-9/\lambda^2}{12-2\left(4-\lambda^2\right)^2}=\frac{\lambda^2-4+\sqrt{\lambda^4-8\lambda^2+10}}{3}. \tag{C6}$$

The solution is between the interval (2.5, 2.6), so we get $\lambda_1\approx 2.59807$.

Appendix D : Experiment details

In this section, we clarify the principle of the optical experiment mentioned in the article. We consider the amplitude of the optical pulse in the n time gap of the m journey $\boldsymbol{a}_n^{(m)}$. The evolution equation for $\boldsymbol{a}_n^{(m)}$ can be derived as follows:

$$\boldsymbol{a}_n^{(m+1)}=\frac{\exp(G)}{3\sqrt{2}}\left[\exp(2\mathrm{i}\theta)\left(\boldsymbol{a}_{n+1}^{(m)}+\boldsymbol{a}_{n-1}^{(m)}\right)+\boldsymbol{U}_n\boldsymbol{a}_n^{(m)}\right], \tag{D1}$$

here

$$\boldsymbol{U}_n=\exp\left(g-\boldsymbol{h}_n^{(\mathrm{AOM})}-\mathrm{i}\boldsymbol{h}_n^{(\mathrm{EOM})}\right), \tag{D2}$$

where $\theta=-2\pi/3$, and G is the gain coefficient of the SOA on the main loop, g is the gain coefficient of the SOA in the center arm of the interferometer, $\boldsymbol{h}_n^{(\mathrm{AOM})}$ is the modulation parameters of AOM in the n-th time slot and $\boldsymbol{h}_n^{(\mathrm{EOM})}$ is the modulation parameter of EOM in the n-th time slot. We can use a waveform generator to drive AOM and EOM independently. Let

$$m=\frac{E}{3\sqrt{2}}\mathrm{e}^{G+2\mathrm{i}\theta}, \tag{D3}$$

$$\boldsymbol{a}_n^{(m)}=\boldsymbol{\mu}^m\boldsymbol{\psi}_n, \tag{D4}$$

so we get

$$E\boldsymbol{\psi}_n=\boldsymbol{\psi}_{n+1}+\boldsymbol{\psi}_{n-1}+\boldsymbol{V}_n\boldsymbol{\psi}_n, \tag{D5}$$

here

$$\boldsymbol{V}_n=\boldsymbol{U}_n\mathrm{e}^{-2\mathrm{i}\theta}. \tag{D6}$$

So we can let

$$\boldsymbol{h}_n^{(\mathrm{EOM})}=\begin{cases}-2\theta, & n \text{ is odd},\\ -2\theta+\arccos\dfrac{\lambda\cos n\omega+1}{\sqrt{\lambda^2+2\lambda\cos n\omega+1}}, & \\ n \text{ is even}, & \end{cases} \tag{D7}$$

$$\boldsymbol{h}_n^{(\mathrm{AOM})}=\begin{cases}g, & n \text{ is odd},\\ g-\ln\sqrt{\lambda^2+2\lambda\cos n\omega+1}, & n \text{ is even}.\end{cases} \tag{D8}$$

Then we have

$$\boldsymbol{V}_n=\begin{cases}1, & n \text{ is odd},\\ 1+\lambda\,\mathrm{e}^{\mathrm{i}n\omega}, & n \text{ is even}.\end{cases} \tag{D9}$$

Note that the spectrum of the operator with this potential is shifted by one unit compared to the mosaicized AAH model's spectrum, thus we can obtain the data of the spectrum of model 1.

Appendix E : Calculation of the Lyapunov exponent

Consider the equation

$$\left(\mathrm{e}^{-2g}\mathrm{e}^{-\mathrm{i}n\alpha}+\mathrm{e}^{2g}\mathrm{e}^{\mathrm{i}n\alpha}\right)\boldsymbol{v}_n+\lambda E\,\mathrm{e}^{\mathrm{i}\theta}\boldsymbol{v}_{n-1}=(E^2-2)\boldsymbol{v}_n, \tag{E1}$$

equivalently,

$$\frac{\boldsymbol{v}_{n-1}}{\boldsymbol{v}_n}=\frac{E^2-2-\mathrm{e}^{-g}\mathrm{e}^{-\mathrm{i}n\alpha}-\mathrm{e}^{g}\mathrm{e}^{\mathrm{i}n\alpha}}{\lambda E\,\mathrm{e}^{\mathrm{i}\theta}}, \tag{E2}$$

Thus,

$$\begin{aligned}&L(E)\\&=\lim_{n\to-\infty}-\frac{1}{n_0-n}\log\left|\frac{\boldsymbol{v}_{n_0}}{\boldsymbol{v}_n}\right|\\&=\lim_{n\to-\infty}-\frac{1}{n}\sum_{n=n_0}^{-\infty}\log\left|\frac{\lambda E\,\mathrm{e}^{\mathrm{i}\theta}}{E^2-2-\mathrm{e}^{-2g}\mathrm{e}^{-\mathrm{i}n\alpha}-\mathrm{e}^{2g}\mathrm{e}^{\mathrm{i}n\alpha}}\right|\end{aligned}$$

$$\begin{aligned}
&\to \frac{1}{2\pi}\int_{-\pi}^{\pi}\log\left|\frac{E^2-2-\mathrm{e}^{2g+\mathrm{i}q}-\mathrm{e}^{-2g-\mathrm{i}q}}{\lambda E}\right|\mathrm{d}q\\
&= -\log|\lambda E|-2g+\frac{1}{2\pi}\int_{-\pi}^{\pi}\log\left|\mathrm{e}^{4g+2\mathrm{i}q}-E\,\mathrm{e}^{2g+\mathrm{i}q}+1\right|\mathrm{d}q\\
&= -\log|\lambda E|+\max\left\{2g,2\left|\operatorname{Im}\arccos\frac{E}{2}\right|\right\}. \qquad \text{(E3)}
\end{aligned}$$

Acknowledgment

Project supported by the National Natural Science Foundation of China (Grant No. 12301218).

References

[1] Anderson P W 1958 *Phys. Rev.* **109** 1492
[2] Abrahams E, Anderson P W, Licciardello D C and Ramakrishnan T V 1979 *Phys. Rev. Lett.* **42** 673
[3] Kondov S S, McGehee W R, Zirbel J J and DeMarco B 2011 *Science* **334** 66
[4] Jendrzejewski F, Bernard A, Muller A, Cheinet P, Josse V, Piraud M, Pezze L, Sanchez-Palencia L, Aspect A and Bouyer P 2011 *Nat. Phys.* **8** 398
[5] Semeghini G, Landini M, Castilho P, Roy S, Spagnolli G, Trenkwalder A, Fattori M, Inguscio M and Modugno G 2014 *Nat. Phys.* **11** 545
[6] Biddle J and Sarma S D 2010 *Phys. Rev. Lett.* **104** 070601
[7] Aubry S and Andre G 1980 *Annales de l'Institut Henri Poincare* **40** 197
[8] Evers F and Mirlin A D 2008 *Rev. Mod. Phys.* **80** 1355
[9] Jiang S, Liu Y and Lang L 2023 *Chin. Phys. B* **32** 097204
[10] Tang Q and He Y 2023 *Chin. Phys. B* **32** 127202
[11] Liu T and Cheng S 2023 *Chin. Phys. B* **32** 027102
[12] Li J, Gong Z and Zhang X 2018 *Phys. Rev. X* **8** 031079
[13] Liu T, Guo H, Pu Y and Longhi S 2020 *Phys. Rev. B* **102** 024205
[14] Longhi S 2019 *Phys. Rev. B* **100** 125157
[15] Prodan E, Hughes T L and Bernevig B A 2010 *Phys. Rev. Lett.* **105** 115501
[16] Tran D T, Dauphin A, Goldman N and Gaspard P 2015 *Phys. Rev. B* **91** 085125
[17] Irsigler B, Zheng J H and Hofstetter W 2019 *Phys. Rev. Lett.* **122** 010406
[18] Gebert U, Irsigler B and Hofstetter W 2020 *Phys. Rev. A* **101** 063606
[19] Ulcakar L, Mravlje J and Rejec T 2020 *Phys. Rev. Lett.* **125** 216601
[20] Avila A 2015 *Acta Mathematica* **215** 1
[21] Avila A, Jitomirskaya S and Sadel C 2014 *J. Eur. Math. Soc.* **16** 1915
[22] Caio M D, Moller G, Cooper N R and Bhaseen M 2019 *Nat. Phys.* **15** 257
[23] Song F, Yao S and Wang Z 2019 *Phys. Rev. Lett.* **123** 246801
[24] Bourgain J and Jitomirskaya S 2002 *J. Stat. Phys.* **108** 1203
[25] Bianco R and Resta R 2011 *Phys. Rev. B* **84** 241106
[26] Longhi S 2019 *Phys. Rev. B* **100**(X) 125157